Visible-light photocatalysis with mullite-type Bi2(Al1-xFex)4O9: Striking the balance between bandgap narrowing and conduction band lowering

Journal:	*ACS Catalysis*
Manuscript ID	cs-2018-012103.R3
Manuscript Type:	Article
Date Submitted by the Author:	n/a
Complete List of Authors:	Curti, Mariano; Departamento de Química, Facultad de Ciencias Exactas y Naturales, Universidad Nacional de Mar del Plata, Kirsch, Andrea; University of Bremen, Institute of Inorganic Chemistry and Crystallography Granone, Luis; Leibniz Universität Hannover, Institut für Technische Chemie Tarasi, Facundo; Universidad Nacional de Mar del Plata, Departamento de Química López Robledo, Germán; Universidad Nacional de Mar del Plata, Bahnemann, Detlef; Universitaet Hannover, Institut für Technische ChemieCallinstraße 3 Murshed, M. Mangir; University Bremen, Institute of Inorganic Chemistry and Crystallography Gesing, Thorsten; Universität Bremen , Institut für Anorganische Chemie Mendive, Cecilia; Universidad Nacional de Mar del Plata, Departamento de Química

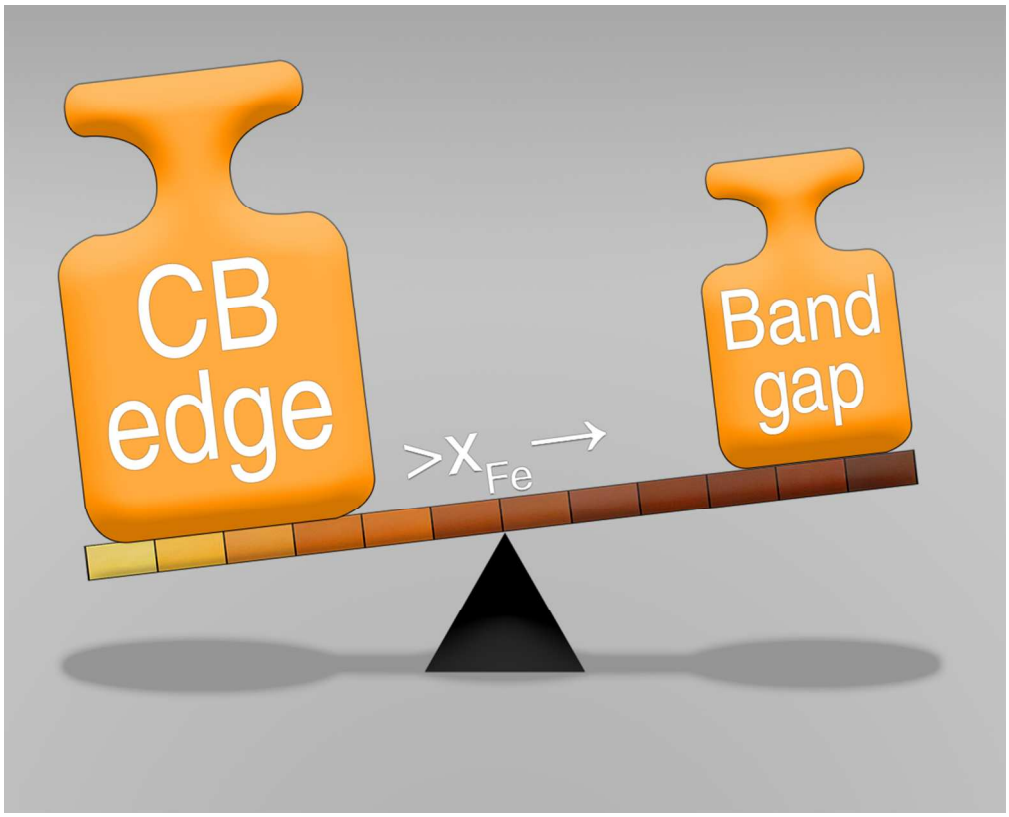

99x80mm (300 x 300 DPI)

Visible-light photocatalysis with mullite-type $Bi_2(Al_{1-x}Fe_x)_4O_9$: Striking the balance between bandgap narrowing and conduction band lowering

Mariano Curti,[1,2] Andrea Kirsch,[3] Luis I. Granone,[4,5] Facundo Tarasi,[1] Germán López Robledo,[1] Detlef W. Bahnemann,[4,5,6] M. Mangir Murshed,[3,7] Thorsten M. Gesing,[3,7] Cecilia B. Mendive[1,2*]

[1] Departamento de Química, Facultad de Ciencias Exactas y Naturales, Universidad Nacional de Mar del Plata, Dean Funes 3350, 7600 Mar del Plata, Argentina.

[2] IFIMAR, CONICET / Facultad de Ciencias Exactas y Naturales, Universidad Nacional de Mar del Plata, Dean Funes 3350, 7600 Mar del Plata, Argentina.

[3] University of Bremen, Institute of Inorganic Chemistry and Crystallography, Leobener Strasse 7, D-28359 Bremen, Germany.

[4] Institute for Technical Chemistry, Leibniz University Hannover, Callinstr. 3, 30167 Hannover, Germany.

[5] Laboratory of Nano- and Quantum-Engineering (LNQE), Wilhelm Leibniz University Hannover, Schneiderberg 39, D-30167 Hannover, Germany.

[6] Laboratory for Nanocomposite Materials, Department of Photonics, Faculty of Physics, Saint-Petersburg State University, Ulianovskaia str. 3, Peterhof, Saint-Petersburg, 198504, Russian Federation.

[7] University of Bremen, MAPEX Center for Materials and Processes, Bibliothekstrasse 1, D-28359 Bremen, Germany.

* Corresponding author, email: cbmendive@mdp.edu.ar

Abstract

The rich crystal chemistry of mullite-type $Bi_2M_4O_9$ (M=Fe, Al, Ga) offers multiple potential applications. In particular, the strong absorption of visible light shown by $Bi_2Fe_4O_9$ has led to an influx of research on its photocatalytic properties. However, most of the published studies deal with the decolorization of dyes and take it as proof of its photocatalytic activity; furthermore, there are no reports on its conduction and valence band edges, and thus the actual redox characteristics of the photogenerated charge carriers have not been determined.

Here we evaluate the photocatalytic activity towards methanol oxidation under monochromatic visible light (λ = 450 nm) irradiation of 12 different members of the $Bi_2(Al_{1-x}Fe_x)_4O_9$ (x = 0 – 1) series of compounds. The reaction rate reaches its highest value at an iron fraction of x = 0.1, while the compounds with the highest iron fractions present negligible activity. Based on an extensive characterization which included the Rietveld refinement of the XRD patterns, the measurement of the specific surface areas by the BET method, and the determination of the flat-band potentials by the Mott–Schottky method, we rationalize the results on the basis of two opposing factors: the incorporation of iron narrows the fundamental bandgap and thus improves light capture, but at the same time it lowers the conduction band edge, hindering the oxygen reduction half-reaction and thus promoting electron–hole recombination. Our work highlights the importance of a proper band edge engineering for photocatalytic applications and underlines the inadequacy of dye decolorization tests for visible light active materials.

Graphical Abstract

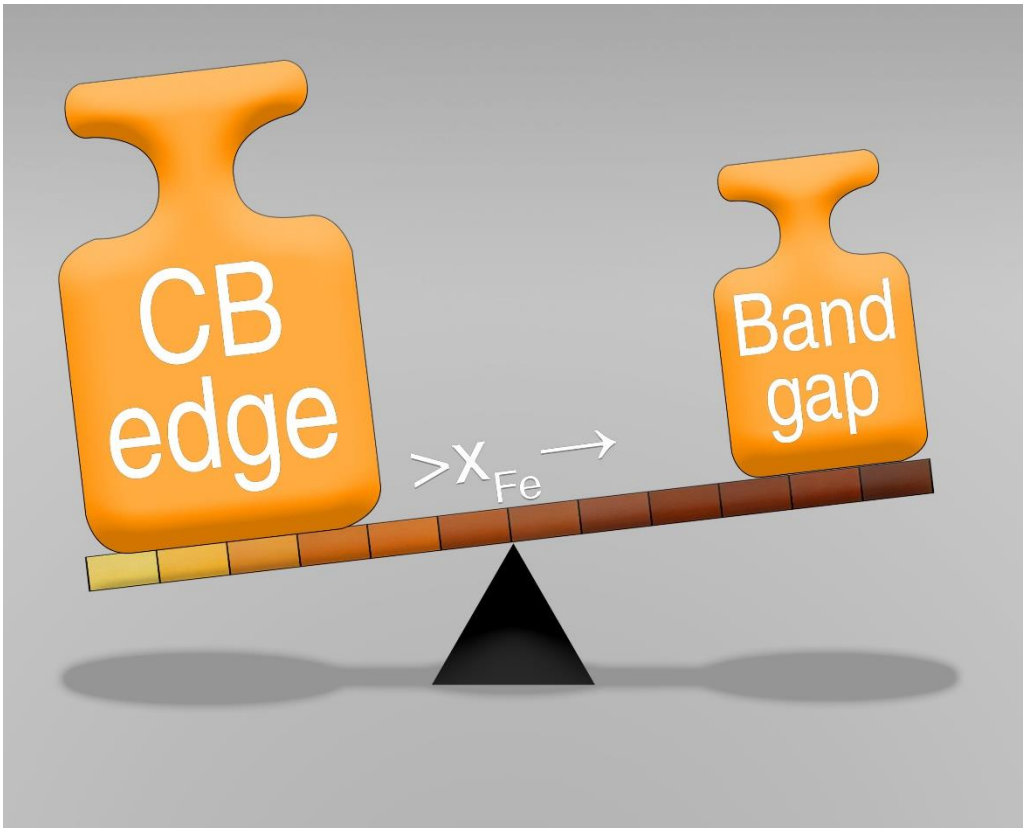

Keywords

Heterogeneous photocatalysis – Methanol oxidation – Mullite-type materials – Band-edge tuning – Bandgap narrowing

1. Introduction

Since the report by Frank and Bard[1] on the photocatalytic oxidation of aqueous cyanide in 1976, a plethora of work has been dedicated to photocatalytic materials as promising candidates for environmental remediation.[2] The main difficulty, i.e., the preparation of low cost, low toxicity materials with a significant visible-light response, still remains unsolved.[3] Mullite-type[4] $Bi_2Fe_4O_9$, a material with interesting crystal-chemical,[5–9] thermal,[10] magnetic,[11] and stereochemically active lone electron pair behavior,[12] has been the subject of numerous studies regarding its photocatalytic activity under visible light irradiation. The material is composed of earth-abundant elements with low toxicity, and shows a very broad absorption in the visible region.[13] It is, thus, a promising material for photocatalytic applications. However, in line with an increasing trend from recent years,[14] most of the reports use the decolorization rate of dyes as a measure of its photocatalytic activity, with only a few exceptions.[15,16]

Though the study of dye mineralization may be of interest for the particular goal of environmental remediation by their specific removal, the decolorization rate gives little to no information on the activity of photocatalysts *per se*: i) the dye decolorization efficiency is usually poorly correlated with the dye mineralization efficiency;[17] ii) the possibility of a sensitization mechanism, where adsorbed dye molecules absorb light and inject electrons into the semiconductor, may lead to the degradation of the dye regardless of whether the semiconductor is actually photocatalytically active;[18,19] and iii) the formation of colored intermediates can obscure the observed kinetic profiles.[20] In addition to this problem, the valence and conduction band edge positions have not yet been determined for $Bi_2Fe_4O_9$, causing a serious gap in the understanding of its photoactivity, since they define the reductive and oxidative power of the photogenerated electrons and holes, respectively.[21]

Here we study the photocatalytic properties of the $Bi_2(Al_{1-x}Fe_x)_4O_9$ series of compounds (x = 0 – 1), which has earlier been reported to be possible in the whole solution range.[5] We determine the crystalline properties, which play an important role on the physical properties of this type of compounds,[22] by Rietveld refinements of their X-ray diffraction patterns; their light absorption properties by diffuse reflectance UV-Vis spectroscopy; their specific surface areas by the BET method; and their flat-band potentials by the Mott–Schottky

method. Finally, we evaluate their visible-light photocatalytic activity by monitoring the formation rate of formaldehyde produced by the visible light oxidation of aqueous methanol.

2. Experimental Procedures

Mullite-type $Bi_2(Al_{1-x}Fe_x)_4O_9$ solid solutions were prepared by a previously reported polyol method.[23] First, a 5.0 wt% solution of polyvinyl alcohol (Sigma-Aldrich Mowiol® 40-88, average molar weight ~205000 g mol^{-1}) was prepared by stirring the solid in water at 353 K. Then $Bi(NO_3)_3 \cdot 5H_2O$ (Sigma-Aldrich, ≥98%) was added to the solution. The addition of a small volume of HNO_3 (3 mL) was necessary to promote the dissolution of $Bi(NO_3)_3 \cdot 5H_2O$. Finally, $Fe(NO_3)_3 \cdot 9H_2O$ and/or $Al(NO_3)_3 \cdot 9H_2O$ were added in stoichiometric amounts to obtain the desired compositions. The starting solution volume was in all cases 38 ml. A 3:1 hydroxyl groups to metal cations ($–OH:M^{3+}$) ratio was used; for clarity, the amounts of reagents used for each composition are detailed in Table S1. The mixture was stirred at 353 K until NO_x evolution stopped. The obtained foam was subsequently dried in an oven at 523 K for 2 hours. This led to a dry foam which was ground in a mortar and finally annealed at 873 K for 30 minutes.

X-ray powder diffraction data were collected in Bragg−Brentano geometry on an X'Pert MPD PRO diffractometer (PANalytical GmbH) equipped with Ni-filtered $Cu_{K\alpha1,2}$ radiation ($\lambda_{\alpha1,2}$ = 0.1540598(2) nm, 0.15439(1) nm, 40 kV, 40 mA) and a X'Celerator detector system. The scans were performed from 5 to 85° 2θ with a step width of 0.0167° 2θ and a measurement time of 175 s per step. The powder data were refined using the Rietveld method (TOPAS V4.2, Bruker AXS). For profile fitting, the fundamental parameter approach was used. The fundamental parameters were fitted against a LaB_6 standard material. The XRD patterns are shown in Figure S1.

The scanning electron microscopy (SEM) measurements of the powders were carried out on a JSM-6510 (JEOL GmbH) equipped with an XFlash Detector 410-M (Bruker AXS GmbH) at an acceleration voltage of 20 kV. Cross-sectional SEM morphology images of the $Bi_2(Al_{1-x}Fe_x)_4O_9$ films were made in secondary electron contrast employing a JSM-

6700F (JEOL GmbH) microscope at 2kV. High resolution transmission electron microscopy (HRTEM) was done with a Talos F200X microscope operated at 200 keV.

X-ray photoelectron spectroscopy (XPS) experiments were carried out with a SPECS instrument. Spectra were acquired using a monochromatic $Al_{K\alpha}$ (1486.6 eV) operating at 100 W and 10 keV. The spectrometer is equipped with a SPECS IQE 12/38 Ar^+ gun, an automatic sample charge neutralization FG 15/40 to ensure a uniform sample space charge, a dual anode Al/Ag X-ray source, and a hemispherical electron energy analyzer. All bands were fitted with Gaussian functions, while the binding energies are referenced to the C 1s line at 284.4 eV.

UV-Vis diffuse reflectance spectra were collected on a Shimadzu UV-Vis spectrophotometer UV-2700 equipped with a UV-Vis DiffuseIR cell from Pike Technologies. Barium sulfate was used as a reference. The data were collected from 190 to 850 nm in 1 nm steps with a medium scanning rate.

Specific surface areas were measured by the single-point Brunauer-Emmett-Teller (BET) method using nitrogen as adsorbate in a Flowsorb II 2300 (Micromeritics Instrument Company). The samples were degassed at 423 K for 30 minutes before performing the measurements.

Flat-band potentials were determined by means of electrochemical impedance spectroscopy using a Zennium Electrochemical Workstation (Zahner-Elektric Company). For these measurements, electrodes of the $Bi_2(Al_{1-x}Fe_x)_4O_9$ samples were prepared by the doctor blade technique using fluoride doped tin oxide (FTO) conductive glasses as substrates. The paste used for the film preparation consisted of 200 mg of the powder sample ground in a mortar along with 100 µl of Triton X-100 (Sigma-Aldrich), 100 mg of polyethylene glycol 1000 (Merck), and 400 µl of deionized water. For the electrochemical measurements, a three-electrode electrochemical cell with a platinum counter electrode and an Ag/AgCl/KCl (3 mol L^{-1}) reference electrode was used. Impedance measurements were carried out at a frequency of 25 Hz in a pH 6.88 buffer solution (0.025 mol L^{-1} KH_2PO_4 and 0.025 mol L^{-1} Na_2HPO_4, Carl Roth) containing 1.0 mmol L^{-1} $K_4[Fe(CN)_6]$ (Merck), 1.0 mmol L^{-1} $K_3[Fe(CN)_6]$ (Merck), and 0.1 mol L^{-1} KCl (Carl Roth) as the electrolyte. Deviations were obtained by averaging the determined flat-band potential for three different films per sample.

An acrylic reactor was used throughout the photocatalytic experiments. Two 3-watts royal blue (λ = 450 nm; emission spectrum shown in Figure S7) LEDs were used as the excitation source. A light intensity of 80 mW cm^{-2} was estimated within the reactor based on UV-LED-meter measurements (Dr. Hönle AG). A volume of 60.0 mL of a 1.0 mol L^{-1} methanol solution in water was used, together with a 3.33 g L^{-1} concentration of the corresponding $Bi_2(Al_{1-x}Fe_x)_4O_9$ compound. Suspensions were magnetically stirred; the resulting pH was between 6.5 and 6.9. The reactor was closed in a loose way to prevent the depletion of the oxidizing agent (atmospheric oxygen). Given the small conversion fractions its concentration was not expected to deviate significantly from its aqueous solubility value of 0.26 mM at 298.15 K.[24] At regular intervals, 2.0 mL aliquots were taken from the reactor and stored in centrifuge tubes. The formation of formaldehyde was assessed by a colorimetric reaction:[25] first the aliquots were centrifuged at 233 Hz, and then 1.5 mL of the supernatant were mixed with the same volume of Nash's reagent (2 mol L^{-1} ammonium acetate, 0.05 mol L^{-1} acetic acid, and 0.02 mol L^{-1} acetylacetone). After a 15 minutes incubation period at 323 K, the concentration of formaldehyde was assessed by UV-visible spectroscopy using an Agilent 8453 spectrophotometer. An absorption coefficient of $\varepsilon_{412\ nm}$ = 7600 mol^{-1} L cm^{-1} was assumed for the resulting colored compound.[26] A single degradation experiment was performed for x_{Fe} = 0.9, 0.8, 0.7, 0.5, and 0.4; duplicate measurements were performed for x_{Fe} = 1.0, 0.3, 0.2, and 0.05; and triplicate measurements were performed for x_{Fe} = 0.6, 0.1, and 0.0. A blank experiment was performed by triplicate in the same way in which degradations were made, excluding the presence of the photocatalyst. A control experiment was also performed using a suspension containing $Bi_2Fe_4O_9$ and a 1 M methanol solution with formaldehyde added to reach a 15 μM concentration. After stirring in the dark overnight we found no significant change in the formaldehyde concentration in solution. This means that formaldehyde is not strongly adsorbed to the $Bi_2Fe_4O_9$ surface and thus we rule out that formic acid or carbon dioxide may be produced by the oxidation of strongly bound formaldehyde without the latter being detectable in solution. Upon irradiation of the system not only formaldehyde is not consumed but instead it is newly produced at a rate consistent with the experiments performed in the absence of an initial supply of formaldehyde. We therefore conclude, in

line with previous findings,[27] that the oxidation of methanol proceeds only to formaldehyde and not further to formic acid or carbon dioxide given a small conversion fraction.

3. Results and Discussion

3.1 Rietveld Refinement of XRD Measurements

The photocatalytic activity of a given material is influenced by many of its physical properties. Consequently, we begin with the characterization of this family of compounds. The phase composition, degree of crystallinity and crystallographic features (average crystallite sizes and lattice parameters) of the mullite-type $Bi_2(Al_{1-x}Fe_x)_4O_9$ samples were determined by Rietveld refinements[28] of their X-ray diffraction patterns. The results are summarized in Table 1 and their dependence on the Fe fraction is shown in Figure 1. In most samples we observed, in conjunction with the mullite-type phase, perovskite-type $BiFeO_3$, bismuth oxide (β-Bi_2O_3), and iron oxide (Fe_3O_4), as shown in Figure 1b. The latter was present in all samples with Fe contents higher than $x_{Fe} = 0.4$. The perovskite-type $BiFeO_3$ is present for all samples with $x_{Fe} \geq 0.3$, showing a steep increase in fraction until $x_{Fe} = 0.7$. Interestingly, its fraction decreases from 71% to 33% when increasing x_{Fe} from 0.7 to 1.0. β-Bi_2O_3 was present in all samples, with a maximum fraction of 15% for $x_{Fe} = 0.4$. The fraction of mullite-type phase has its lowest point of 20% for $x_{Fe} = 0.7$, and reaches its maximum of 99% for $x_{Fe} = 0.0$. The degree of crystallinity shows an increase with the incorporation of Fe until $x_{Fe} = 0.4$ with a sudden drop at $x_{Fe} = 0.5$ followed by a steep increase until $x_{Fe} = 0.7$ (Figure 1a). The drop in crystallinity might be explained by the concomitant and competing nucleation of $BiFeO_3$ and $Bi_2(Al_{1-x}Fe_x)_4O_9$, since the subsequent steep increase follows the evolution of phase fraction and crystallite size of the perovskite-type phase $BiFeO_3$ (Figure 1a-c).

The diffraction patterns for samples with Fe contents $0.1 \leq x_{Fe} \leq 0.3$ show a second mullite-type phase with different lattice parameters. These patterns were fitted assuming the presence of two different mullite-type phases, explaining the second set of crystallite sizes in Figure 1c in this region. The evolution of the lattice parameters in both of these phases

together with literature data[29] is shown in Figure 1d-f. Since the effective ionic radius of Al^{3+} (53.5 pm[30]) is smaller than that of Fe^{3+} (64.5 pm[30]) the lattice parameter is assumed to increase linearly with the incorporation of Fe into the $Bi_2Al_4O_9$ structure according to Vegard's law.[31] In this study the increase of the lattice parameters is stronger than expected with increasing Fe content following a quadratic rather than a linear behavior. This observation suggests that Fe^{3+} is preferably incorporated into the structure. The observed decrease from $0.5 \leq x_{Fe} \leq 0.7$ can be explained by the increase of the $BiFeO_3$ and Fe_3O_4 fractions in this range, reducing the amount of available Fe^{3+} to be incorporated into $Bi_2(Al_{1-x}Fe_x)_4O_9$. Interestingly, the lattice parameters of the second mullite-type phase appearing at $x_{Fe} = 0.1$ start with similar values to the initial phase and then follow the expected linear trend, similar to the data of Voll et al.[29]

The number of present phases in the resulting powders increases at higher iron contents. This can be rationalized on the basis of the rich phase diagram of the $Bi_2O_3 – Fe_2O_3$ system, which shows many complex features and can be strongly affected by the presence of impurities.[32] The use of a relatively mild calcination step (873 K for 30 minutes) may contribute to the formation of metastable phases ($BiFeO_3$ is metastable with respect to $Bi_2Fe_4O_9$ in the 720 – 1040 K range[33]) and to an incomplete crystallization. However, higher temperatures must be avoided if small crystallites are looked for.[23]

Table 1: X-ray characterization of the $Bi_2(Al_{1-x}Fe_x)_4O_9$ solid solutions. Deviations are shown in brackets.

Nominal composition	Phase fraction / % (crystalline parts only)				Degree of Crystallinity / %	Average crystallite size / nm	
	Mullite-type	Perovskite-type	β-Bi_2O_3	Fe_3O_4		Mullite-type	Perovskite-type
$Bi_2Al_4O_9$	99(5)	--	1(5)	--	38(5)	19(1)	--
$Bi_2(Al_{0.95}Fe_{0.05})_4O_9$	98(5)	--	2(5)	--	38(5)	23(1)	--
$Bi_2(Al_{0.9}Fe_{0.1})_4O_9$	96(5)	--	4(5)	--	44(5)	27(2)	--
$Bi_2(Al_{0.8}Fe_{0.2})_4O_9$	95(5)	--	5(5)	--	59(5)	19(1)	--
$Bi_2(Al_{0.7}Fe_{0.3})_4O_9$	90(5)	--	10(5)	--	61(5)	19(1)	--
$Bi_2(Al_{0.6}Fe_{0.4})_4O_9$	78(5)	7(5)	15(5)	--	66(5)	20(1)	--
$Bi_2(Al_{0.5}Fe_{0.5})_4O_9$	77(5)	20(5)	3(5)	--	40(5)	17(1)	18(1)
$Bi_2(Al_{0.4}Fe_{0.6})_4O_9$	52(5)	35(5)	13(5)	--	76(5)	22(1)	31(1)
$Bi_2(Al_{0.3}Fe_{0.7})_4O_9$	20(5)	71(5)	3(5)	6(5)	97(5)	22(2)	42(1)
$Bi_2(Al_{0.2}Fe_{0.8})_4O_9$	29(5)	58(5)	5(5)	8(5)	93(5)	25(2)	35(2)
$Bi_2(Al_{0.1}Fe_{0.9})_4O_9$	56(5)	26(5)	7(5)	11(5)	92(5)	26(1)	36(2)
$Bi_2Fe_4O_9$	56(5)	33(5)	6(5)	5(5)	90(5)	21(1)	34(1)

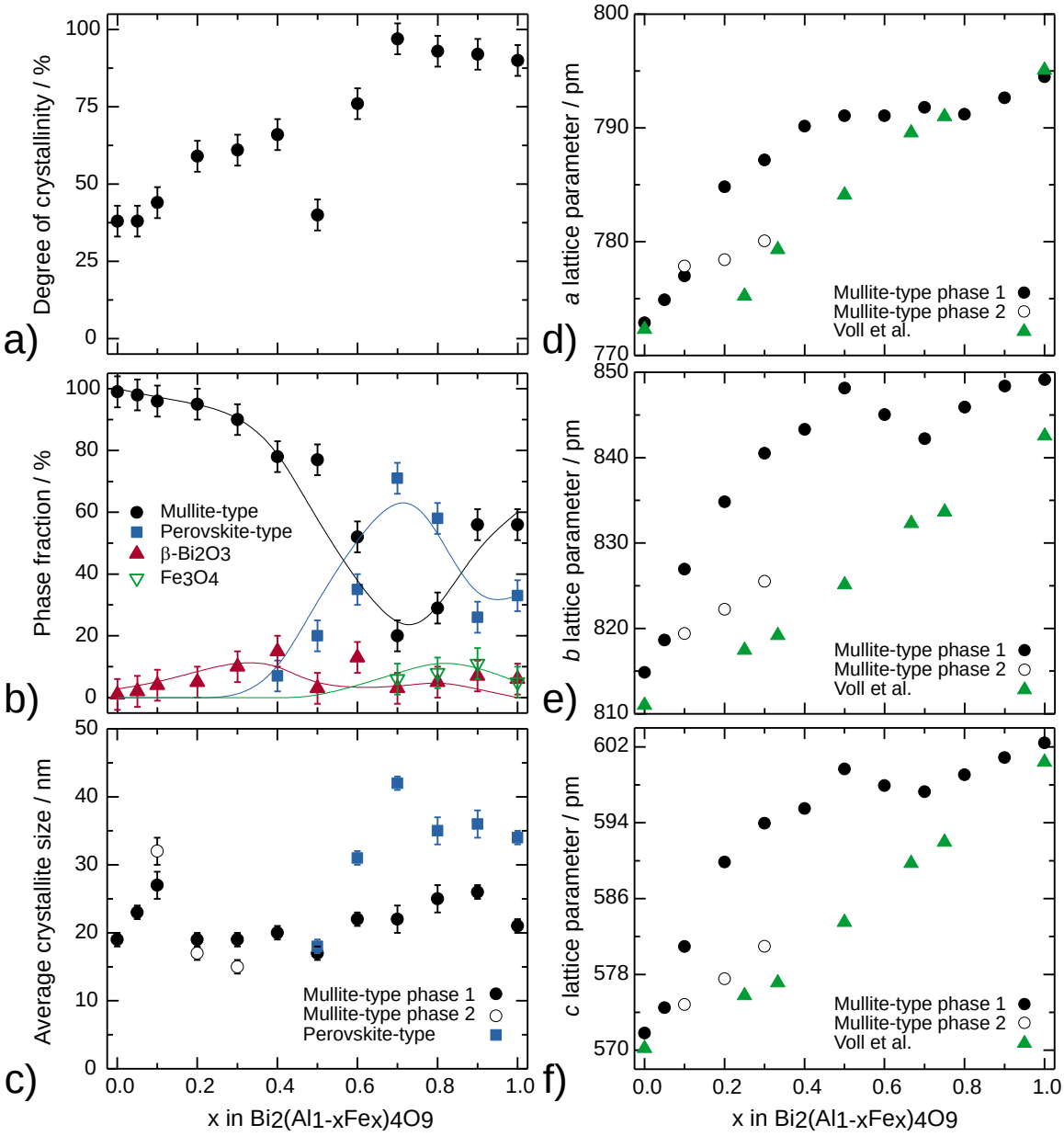

Figure 1: Crystallographic characterization from the Rietveld refinement of the X-ray patterns of the $Bi_2(Al_{1-x}Fe_x)_4O_9$ solid solutions. **a)** Degree of crystallinity. **b)** Crystalline phases fractions. **c)** Average crystallite size of the main phases. **d)** – **f)** a, b and c lattice parameters of the two observed mullite-type phases together with literature data from reference [29]. All lines are guides for the eyes.

3.2 Electron microscopies and XPS analysis

As complementary methods to the Rietveld analysis, we performed scanning electron and transmission electron microscopy measurements (SEM and HRTEM, respectively) of the powdered samples. In Figure S2 we show SEM micrographies of all investigated samples at low magnifications (230X). In all cases, the particles composing the powders show rather irregular shapes, and are polydisperse in size, ranging from a few up to a hundred microns. A certain tendency to form plate-like particles can also be observed. The incorporation of iron does not result in any clear tendency regarding the size and shape of the individual particles and the aggregates.

SEM micrographs at higher magnifications (1800X) of all samples are shown in Figure S3. The tendency of the aggregates to form plate-like particles is more clearly observed in these micrographs, though in all cases more regular shaped (and smaller) particles are abundant. Again, the incorporation of iron does not lead to any apparent change in the size distribution or shape of the particles. As shown in some cases (for instance x_{Fe}=0.5 in Figure S3) some porosity can be observed but does not impact in the overall exposed surface as it will be discussed in Section 3.4.

For the electrochemical characterization of the compounds (Section 3.5) it is necessary to prepare films over conductive substrates. Since the thickness of the films can affect their electronic properties, for meaningful comparisons it is important to achieve a homogeneous thickness both within each film and between different samples. In Figure S4 we show the cross-sectional SEM micrographs of representative samples x_{Fe} = 0.0, 0.1, 0.2, and 1.0. The calculated thicknesses and standard deviations, from 10 measurements along each film edge, are 33±3, 30±4, 35±3, and 37±2 μm, respectively. Therefore, we can rule out the thickness as a factor influencing the comparison of electrochemical properties, since they are constant both throughout each film and among the samples.

The HRTEM micrographs of three representative samples, x_{Fe} = 0.0, 0.1, and 1.0, are shown in Figure S5. For all three samples the crystallite sections are approximately circular in shape, with most of the radii in the 10 to 30 nm range, in very good agreement with the Rietveld analysis. With high magnifications it is possible to estimate the lattice spacings, as shown at the right-hand side of Figure S5. For x_{Fe} = 0.0 (i.e. $Bi_2Al_4O_9$) large crystalline

areas could be observed with a corresponding *d*-spacing of 0.57 nm. This value corresponds to the lattice-plane distance for (001) planes, which is equal to 0.5670 nm and has previously been observed in TEM investigations of $Bi_2Al_4O_9$.[34] At different crystallites a *d*-spacing of 0.33 nm was also observed; this value is in agreement with the corresponding lattice-plane distance for (021) planes, 0.3300 nm.[34] For sample x_{Fe} = 0.1 a similar arrangement of crystallites to the previous case is observed. While different *d*-spacings could be calculated from many individual crystallites, a recurring value of 0.31 nm was visible in large crystalline regions. By using the lattice parameters calculated from the Rietveld analysis we can assign this value to the lattice-plane distance for (121) planes, equal to 0.3091 nm. The investigated sample with x_{Fe} = 1.0 also shows crystallites with diameters between 20 and 30 nm. The *d*-spacings of crystalline regions yielded a value of 0.33 nm, in good agreement with spacings previously assigned to the lattice-plane distance for (201) planes.[13] For different crystallites we also observed *d*-spacings of 0.27 and 0.60, which are in agreement with the lattice-plane distance for (112)[35] and (001)[23] planes, respectively.

The x-ray photoelectron spectroscopy (XPS) analysis of three representative samples (x_{Fe} = 0.0, 0.1, and 1.0) is shown in Figure S6. All three samples show the expected bands for their constituting elements; in particular, bismuth 4f and oxygen 1s bands are clearly visible, while aluminum 2p and iron $2p_{2/3}$ bands have lower intensity due to their lower atomic sensitivity factors. We have analyzed each of the mentioned bands by means of a fitting procedure in order to find the contributions to each one and their exact position. In the case of the Bi $4f_{5/2}/4f_{7/2}$ doublet we found average values of 164.0 and 158.8 eV for each band, in good agreement with the values of 163.8 and 158.5 eV previously observed for $Bi_2Al_4O_9$.[34] In our samples, however, each band is split in two components of similar intensity. The emergence of such bands has been previously linked to a large number of intrinsic defects due to the use of a *fast* synthetic procedure, similar to the one we use here.[34] In the case of sample x_{Fe} = 1.0 the split is larger, which could be related to the presence of perovskite-type $BiFeO_3$, detected by the XRD analysis. Samples x_{Fe} = 0.0 and x_{Fe} = 0.1 (compositionally similar) also show comparable patterns for the oxygen 1s band, with one major component and a minor one. On the contrary, the O 1s band for sample x_{Fe} = 1.0 shows three components of similar weight. The presence of significant fractions of

$BiFeO_3$, Fe_2O_3, and Bi_2O_3 found in this sample via XRD is a plausible explanation for the multiple components. The analysis of the aluminum 2p band in samples containing Al (x_{Fe} = 0.0 and x_{Fe} = 0.1) shows a similar band with two components of similar area, as expected for these two samples in which the chemical environment of Al atoms is similar. The iron 2p band is easily observed in the x_{Fe} = 1.0 sample (i.e. $Bi_2Fe_4O_9$). There are three main bands at 713.5, 721.7, and 726.7 eV, which are in agreement with previous assignments to Fe $2p_{3/2}$, a Fe $2p_{3/2}$ satellite, and Fe $2p_{1/2}$ in $Bi_2Fe_4O_9$.[36,37] The minor bands could also be explained in this case by the presence of $BiFeO_3$ and Fe_2O_3. For the sample with x_{Fe} = 0.1 the Fe 2p bands are rather weak, as expected from the low iron fraction, with two main bands located at 723.9 and 736.8 eV. The considerable difference with respect to sample with x_{Fe} = 1.0 could be explained on the basis of the different chemical environment of iron atoms, which are a minority in the lattice in the case of x_{Fe} = 0.1.

3.3 UV-Vis Spectroscopic Measurements

The UV-Vis spectra of the $Bi_2(Al_{1-x}Fe_x)_4O_9$ powders were taken in the diffuse reflectance mode. Each reflectance spectrum $[R(\lambda)]$ was transformed according to the Kubelka – Munk model[38] to obtain the function $F(R)$, related to the absorption and scattering coefficients $k(\lambda)$ and $s(\lambda)$:

$$F(R) = \frac{[1-R(\lambda)]^2}{2R(\lambda)} = \frac{k(\lambda)}{s(\lambda)} \quad (1)$$

The resulting spectra are shown in Figure 2a. In the investigated range (200 – 850 nm) all compounds show two absorption bands: one centered at ~700 nm, and another at shorter wavelengths, the position of which is highly dependent on the iron content. The only exception is the x_{Fe} = 0.0 compound, which does not show the band at ~700 nm. Although it is currently the subject of a debate,[39] an absorption band in this range for $Bi_2Fe_4O_9$ is generally accepted to be caused by Fe^{3+} *d-d* transitions,[13,15] likely intensified by a strong magnetic coupling between adjacent Fe^{3+} cations[40] that relaxes the doubly-forbidden nature of the transitions. In the present study we observe such band in all samples containing Fe but not in $Bi_2Al_4O_9$, thus supporting the *d-d* transitions hypothesis.

The second absorption band can be attributed to the bandgap of each compound. The spectra of Figure 2a show that the incorporation of iron into the structure leads to a red-shift of this band. Quantum-chemical calculations have shown that the valence band of both

$Bi_2Al_4O_9$ and $Bi_2Fe_4O_9$ have, predominantly, oxygen 2*p* character.[39,41,42] The conduction bands, however, show important differences between the compounds: while that of $Bi_2Al_4O_9$ shows contributions from Bi orbitals, the lower part of the conduction band in $Bi_2Fe_4O_9$ is mainly composed of iron 3*d* orbitals. The availability of low-lying *d* orbitals thus effectively narrows the bandgap in the iron-containing compounds.

Although the crystallographic analysis (Table 1) shows varying amounts of other phases, no others absorption bands due to $BiFeO_3$, Bi_2O_3 or Fe_2O_3 could be detected in our analysis.

The calculation of bandgaps from absorption spectra can be performed by means of the Tauc relationship,[43,44] given by:

$$\alpha(\frac{hc}{\lambda}) \approx B(\frac{hc}{\lambda} - E_g)^n \quad (2)$$

Where h is the Planck constant, c the speed of light, λ the wavelength of the impinging light, E_g the bandgap energy of the material, B a proportionality constant, and n depends on the nature of the transition ($n = 2$ for indirect transitions and $n = 1/2$ for direct transitions). This method can thus be used to calculate bandgap energies as long as the nature of the transition is known. The recently proposed "derivation of absorption spectrum fitting method" (DASF), developed by Souri and Tahan,[45] provides an alternative way of calculating the bandgap width without knowing whether the involved transition is direct or indirect. The data are processed according to the following expression:

$$\frac{d\{\ln[\frac{A(\lambda)}{\lambda}]\}}{d(1/\lambda)} = \frac{n}{(\frac{1}{\lambda} - \frac{1}{\lambda_g})} \quad (3)$$

Where $A(\lambda)$ is the absorbance at a wavelength λ and λ_g is the wavelength corresponding to the bandgap energy. Since the scattering coefficient $s(\lambda)$ in equation (1) can be reasonably assumed to be independent of the wavelength (i.e. $s(\lambda) = s$), the $F(R)$ function can be related to the absorption spectrum $A(\lambda)$:

$$F(R) \sim A(\lambda) \quad (4)$$

Therefore, by plotting the left-hand side of equation (3) as a function of $\frac{1}{\lambda}$, a discontinuity appears at $\lambda = \lambda_g$; by fitting the resulting peaks, the Kubelka – Munk transformed reflectance data can be used to estimate the wavelength of the transitions. This presents a plausible solution to the problem of unknowing n (pointed out by Scaife in 1980[46] and more recently highlighted by Ohtani[19]) as demonstrated by Kirsch et al.[13] It also overcomes the problematic way, as explained by Ohtani,[19] to determine the type of transition of a given material by comparing the direct and indirect Tauc plots, since both usually show linear ranges of similar widths.[47]

We determined the position of the two observed absorption bands at each composition both by the Tauc method (considering the possibilities of direct or indirect bandgaps) and the DASF method. The results for all samples are shown in Figure 2b. Additionally, as an example, the procedure for the bandgap calculations for $Bi_2Fe_4O_9$ are shown in Figure S8. The position of the lower energy band (between 1.5 and 1.7 eV, denoted as "1st band") is relatively independent of the iron content regardless of the method used. Moreover, since the results of the DASF method practically overlap with those of the Tauc method for a direct transition, it is assumed here that these are indeed direct transitions.

Consistently with the spectra of Figure 2a, the Tauc and DASF analyses show that the second absorption band has a strong dependence on the composition: the incorporation of iron leads to a shift to lower energies (i.e. longer wavelengths). Interestingly, the DASF method coincides with the Tauc method for indirect transitions in the $0.0 \leq x_{Fe} \leq 0.2$ range, and with the Tauc method for direct transitions for $0.3 \leq x_{Fe} \leq 1.0$. Our results are in disagreement with those of the theoretical work on $Bi_2Al_4O_9$[42], indicating to a direct semiconductor (to the best of our knowledge, there are no other experimental results). A possible explanation for the observed discrepancy can be explained in terms of the relatively low crystallinity shown by our samples. It is possible that low-energy transitions related to defects, or to amorphous (e.g. domain wall) fractions, could mask the fundamental bandgap of the compounds with low iron contents.

The literature data on $Bi_2Fe_4O_9$ show contradictory results. Many works employ the Tauc method, arbitrarily choosing the transition type to be either direct[16,48] or indirect[49]. The application of the DASF method to well-crystallized samples determined that the involved

transitions are direct;[13] however, theoretical works[39,50] indicate the transitions to be indirect. Our analysis by the Tauc method shows that the transformed spectra can be properly fitted for both cases. However, the match between the DASF method and the Tauc method for direct transitions leads us to conclude that the transitions are direct.

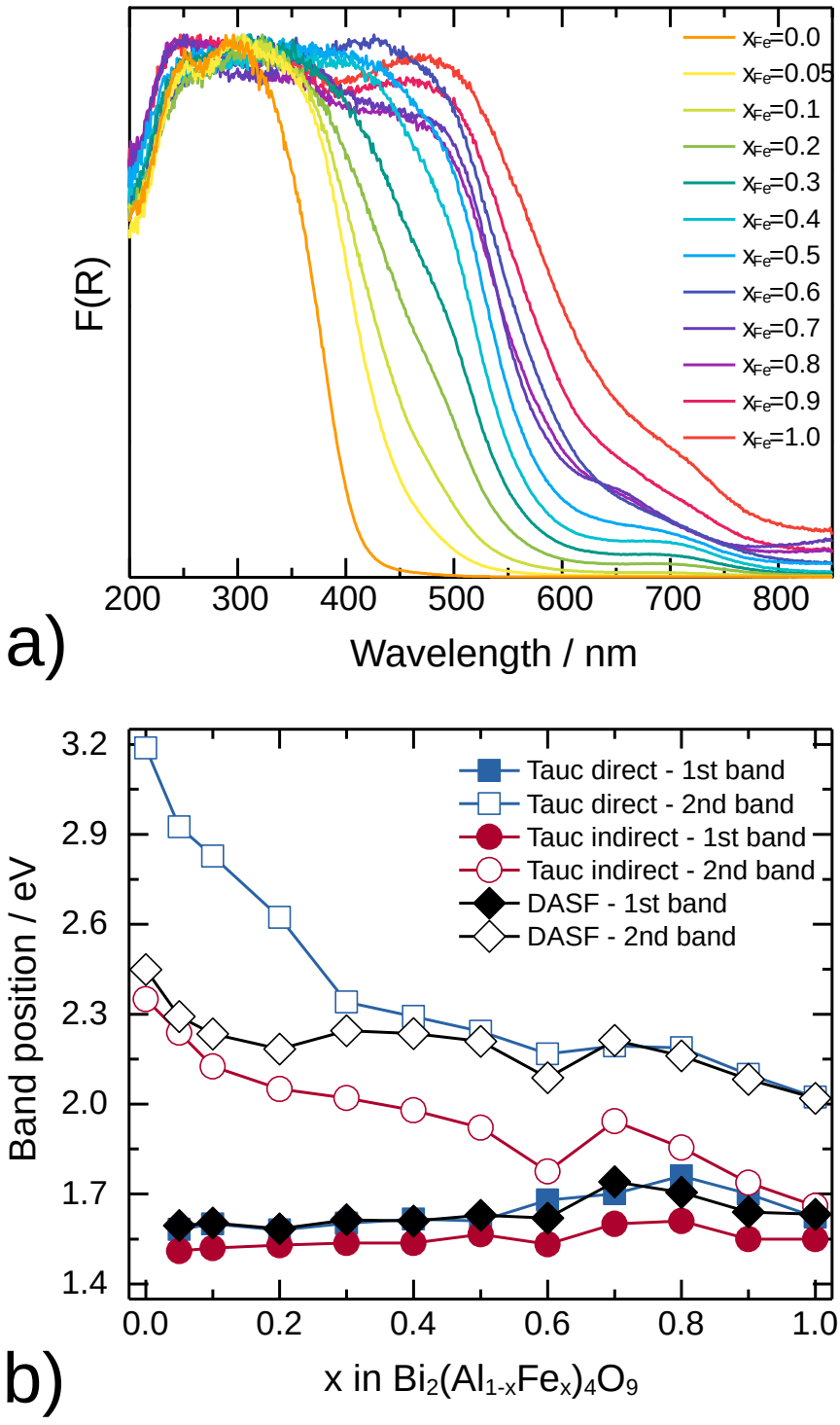

Figure 2: a) Kubelka-Munk transformed diffuse UV-vis spectra of the $Bi_2(Al_{1-x}Fe_x)_4O_9$ solid solutions. **b)** Bandgap determination using the DASF and Tauc methods.

3.4 BET Measurements

The specific surface areas of the $Bi_2(Al_{1-x}Fe_x)_4O_9$ solid solutions are summarized in Table 2. Except for samples with x_{Fe} = 0.0 and 0.2, with specific surface areas of 7.8 and 5.8 $m^2 g^{-1}$ respectively, all values are below 4.4 $m^2 g^{-1}$. As Figure 3 shows, the specific surface areas do not show any systematic trend with increasing iron fractions. In comparison to the widely used photocatalyst Evonik P25, with a specific surface area of 50 $m^2 g^{-1}$,[51] all samples investigated here display relatively low values. Literature data show similar values for $Bi_2Fe_4O_9$, ranging from 0.53 to 15.52 $m^2 g^{-1}$ depending on the synthetic conditions.[15,16,36,52–55] In the case of $Bi_2Al_4O_9$ or intermediate compounds it is not possible to perform any comparison since, to the best of our knowledge, these are the first results regarding their specific surface area.

Table 2: Specific surface areas of the $Bi_2(Al_{1-x}Fe_x)_4O_9$ solid solutions. Deviations, in brackets, were obtained from the average of three successive determinations.

Nominal composition	Specific surface area / $m^2 g^{-1}$
$Bi_2Al_4O_9$	7.8(2)
$Bi_2(Al_{0.95}Fe_{0.05})_4O_9$	2.8(1)
$Bi_2(Al_{0.9}Fe_{0.1})_4O_9$	2.4(2)
$Bi_2(Al_{0.8}Fe_{0.2})_4O_9$	5.8(2)
$Bi_2(Al_{0.7}Fe_{0.3})_4O_9$	3.5(2)
$Bi_2(Al_{0.6}Fe_{0.4})_4O_9$	3.2(1)
$Bi_2(Al_{0.5}Fe_{0.5})_4O_9$	3.2(1)
$Bi_2(Al_{0.4}Fe_{0.6})_4O_9$	3.4(1)
$Bi_2(Al_{0.3}Fe_{0.7})_4O_9$	2.5(2)
$Bi_2(Al_{0.2}Fe_{0.8})_4O_9$	4.2(2)
$Bi_2(Al_{0.1}Fe_{0.9})_4O_9$	4.2(1)
$Bi_2Fe_4O_9$	4.4(1)

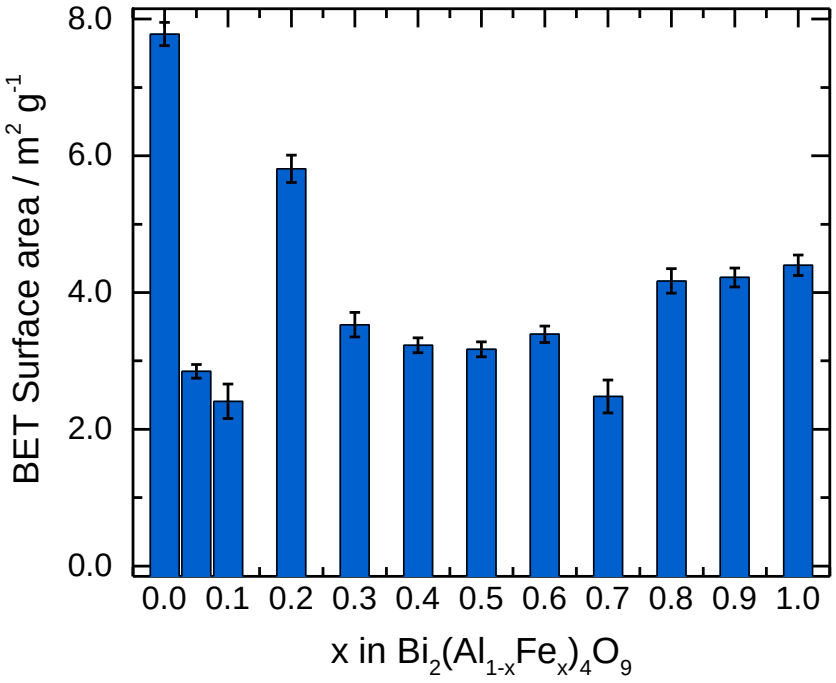

Figure 3: Specific surface areas of the $Bi_2(Al_{1-x}Fe_x)_4O_9$ solid solutions represented versus Fe fractional content, as determined by the Brunauer – Emmett – Teller (BET) method.

3.5 Flat-band Potential Measurements

Among the different physicochemical properties of a photocatalytic material, the positions of the conduction and valence band edges are of fundamental importance, since they offer information on the reductive and oxidative capabilities of the photogenerated electrons and holes, respectively. Yet, to the best of our knowledge, there are no published reports of experimental measurements for mullite-type compounds. We determined the flat-band potential of the $Bi_2(Al_{1-x}Fe_x)_4O_9$ solid solutions by analyzing the potential (U) dependence of the space charge layer capacitance (C_{scl}). The relationship between C_{scl} and U is given by the Mott–Schottky equation:[56]

$$\frac{1}{C_{scl}^2} = \frac{2}{qN_d\varepsilon\varepsilon_0}\left(U - U_{fb} - \frac{kT}{q}\right) \quad (5)$$

Where q is the elementary charge, N_d is the donor density, $\varepsilon\varepsilon_0$ is the permittivity of the semiconductor, U_{fb} is the flat-band potential, k is the Boltzmann constant, and T is the temperature.

We determined C_{scl} by fitting the impedance data collected from -0.15 to 0.55 V vs. RHE (Reversible Hydrogen Electrode) to an equivalent Randles circuit (inset of Figure 4a). Please note that reduction potentials measured against the RHE can be referred to the Normal Hydrogen Electrode (NHE) by subtracting 0.0591 V · pH to their value. Due to the linear relationship between the reciprocal square of C_{scl} and the potential, the flat-band potential was determined by extrapolating the Mott–Schottky plot ($1/C_{scl}^2$ vs. U) to the intercept with the x-axis (Figure 4a). The observed positive slopes indicate that the samples show n-type conductivity. In general, oxides tend to be n-type, since the formation of O^{2-} vacancies is usually favored with respect to the formation of cationic vacancies.[57]

The flat-band potentials of the $Bi_2(Al_{1-x}Fe_x)_4O_9$ compounds together with the redox potential for the one-electron reduction of oxygen (0.13 V vs RHE[58]) are shown in Figure 4b. As the iron content of the samples increases, flat-band potentials shift to more positive values vs. RHE. As discussed in the spectroscopic characterization, the incorporation of iron lowers the conduction band edge by introducing Fe 3*d* states. The Mott–Schottky analysis shows that while decreasing the bandgap of the material, this also results in a lower reductive power of the photogenerated electrons. As Figure 4b shows, the electron transfer from the conduction band of the semiconductor to dissolved oxygen molecules becomes thermodynamically unfavorable as x_{Fe} increases. The situation is similar to that of hematite (α-Fe_2O_3), which shows a small bandgap but is unable to reduce O_2[59] due to its conduction band edge being at higher positive potentials (~ 0.4 V vs. RHE as determined by the Mott–Schottky method[60]).

Previous works[16,35] have assumed a conduction band edge of -0.6 V vs. RHE for $Bi_2Fe_4O_9$, based on Density Functional Theory calculations.[15] However, those calculations were performed under three-dimensional periodic boundary conditions, where the computed band edge energies are shifted by an unknown value due to the usage of the Ewald summation method.[61] Therefore, meaningful results for the band positions can only be

obtained by means of slab (semi-infinite surface) calculations,[62] and are yet to be found for these compounds.

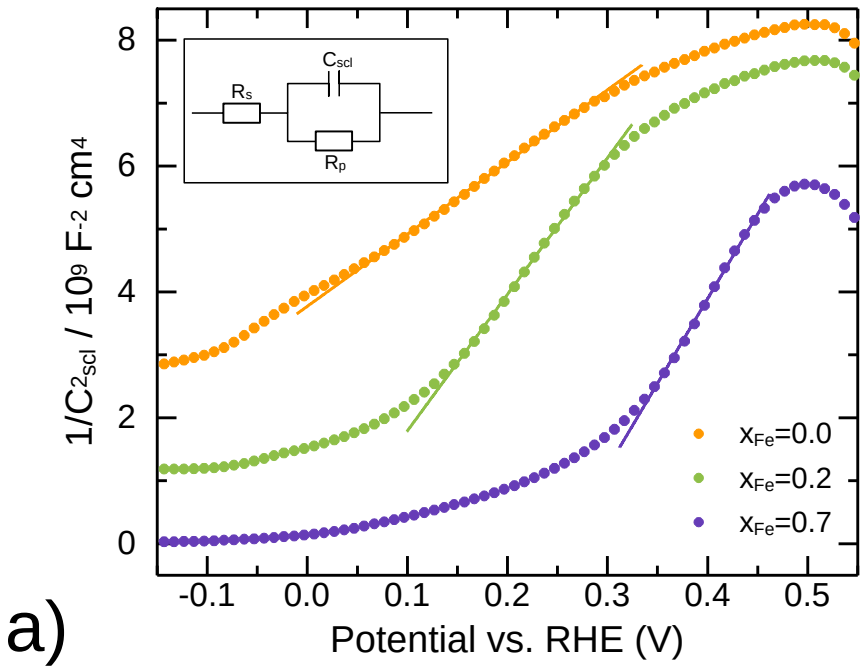

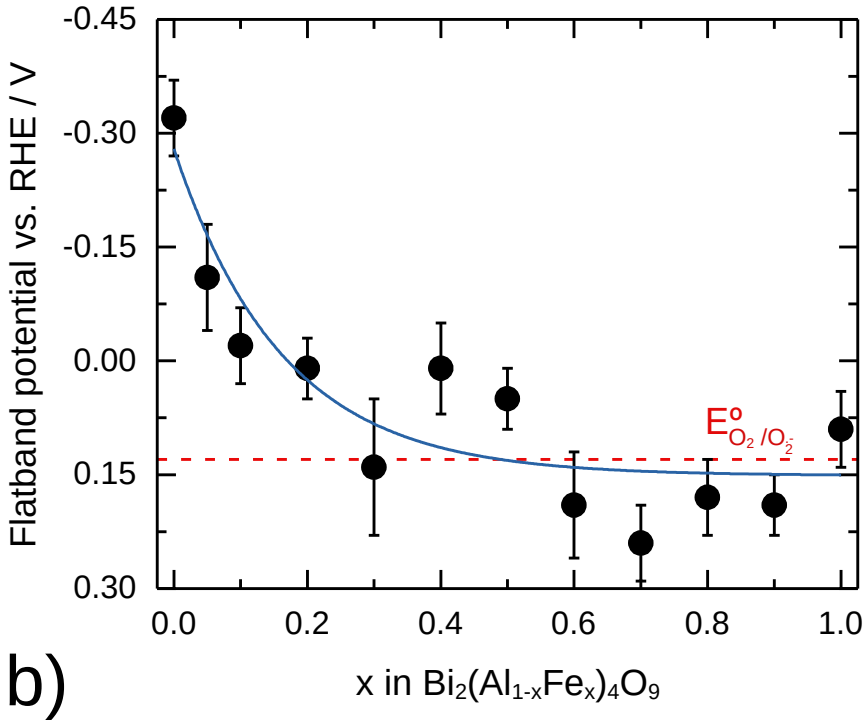

Figure 4: **a)** Mott-Schottky plots of the $Bi_2(Al_{1-x}Fe_x)_4O_9$ solid solutions with x_{Fe} = 0.0, 0.2, and 0.7. The inset shows the equivalent Randles circuit used to fit the electrochemical impedance data, where R_s is the total series resistance, R_p is the parallel resistance due to the charge transfer, and C_{scl} is the space-charge layer capacitance. **b)** Flat-band potentials of the $Bi_2(Al_{1-x}Fe_x)_4O_9$ solid solutions represented versus x_{Fe}. The red dashed line corresponds to the redox potential for the one-electron reduction of oxygen in water,[58] while the blue solid line shows the fitting to an exponential function.

3.6 Photocatalytic Measurements

To evaluate the photocatalytic activity of the $Bi_2(Al_{1-x}Fe_x)_4O_9$ compounds we chose the oxidation of aqueous methanol in air as the test reaction. Since methanol is colorless, its visible light photo-oxidation can be unambiguously assigned to the action of the photocatalyst, contrarily to the widely used dye decolorization tests.[20] At the same time, formaldehyde, the first oxidation product of methanol, can be easily monitored by UV-Vis spectroscopy after its derivatization with the Nash reagent.[25]

The kinetic profiles for the formation of formaldehyde are shown in Figure 5. Another positive aspect of the chosen test reaction is evident in this figure since the kinetic profiles follow a linear trend (i.e. apparent zero-order kinetics) in all cases. The mechanism of this reaction has been well studied over TiO_2 photocatalysts.[26,63,64] In principle, the same mechanism might be operative when using $Bi_2(Al_{1-x}Fe_x)_4O_9$ solid solutions:

$$Bi_2(Al_{1-x}Fe_x)_4O_9 \xrightarrow{h\nu} h^+_{VB} + e^-_{CB} \quad (6a)$$

$$h^+_{VB} + e^-_{CB} \rightarrow Bi_2(Al_{1-x}Fe_x)_4O_9 + heat \quad (6b)$$

$$h^+_{VB} + CH_3OH \rightarrow CH_2OH^{\cdot} + H^+ \quad (6c)$$

$$e^-_{CB} + O_2 \rightarrow O_2^{\cdot -} \quad (6d)$$

$$CH_2OH^{\cdot} + O_2 \rightarrow OOCH_2OH^{\cdot} \rightarrow HCHO + H^+ + O_2^{\cdot -} \quad (6e)$$

$$2O_2^{\cdot -} + 2H^+ \rightarrow H_2O_2 + O_2 \quad (6f)$$

Upon the generation of an electron-hole pair (reaction (6a)), if recombination (reaction (6b)) is avoided, the oxidizing hole is captured by methanol (reaction (6c)), while the

electron on the conduction band reduces O_2 from air (reaction (6d)). The hydroxymethyl radical formed in reaction (6c) is highly reductive, and thus in the presence of air it reduces O_2 to form $OOCH_2OH^{\cdot}$, which rapidly decomposes to generate formaldehyde, $HCHO$. The superoxide radicals $O_2^{\cdot-}$ formed in reactions (6e) and (6f) can recombine to form hydrogen peroxide, H_2O_2, which may either accumulate or react with newly photogenerated charge carriers depending on its concentration.

The expected global reaction from the mechanism is:

$$CH_3OH + O_2 \xrightarrow{h\nu} HCHO + H_2O_2 \quad (7)$$

Therefore, under our reaction conditions the expected ratio between produced formaldehyde and consumed methanol is 1:1. The formation of H_2O_2, which also follows a 1:1 ratio with formaldehyde, has been demonstrated in the methanol/TiO_2 system by means of the catalase enzyme.[26] Catalase is able to decompose H_2O_2, simultaneously yielding a second molecule of formaldehyde. Thus for each photogenerated electron-hole pair two formaldehyde molecules could be produced. In our case the maximum expected H_2O_2 concentration is in the μM range, hence it is reasonable to assume that its production does not affect the behavior of the photocatalytic system. Similarly, although formaldehyde could in principle be further oxidized to formic acid ($HCOOH$) or carbon dioxide (CO_2), we employ a concentration of methanol high enough (1.0 mol L^{-1}) to avoid a significant conversion fraction during the irradiation period, and thus methanol, present in a large excess, is preferentially oxidized. For the same reason the kinetic profiles follow pseudo zero-order kinetics.[26,65] The formation of formic acid or carbon dioxide has only been observed in systems were a significant fraction of methanol is oxidized, for example by Selli et al.[66] This is because the hole scavenging power of methanol is, although somewhat lower, comparable to that of formaldehyde and formic acid.[67] Therefore, the fact that methanol concentration is at least 4 orders of magnitude larger than that of formaldehyde during the entire photocatalytic run means that it will be preferentially oxidized due to kinetic reasons.

We note that in some cases the formaldehyde concentration at the beginning of the irradiation is slightly displaced from the origin to positive values. This may correspond to a

slight decomposition of the starting methanol solution. However, by performing duplicate and triplicate measurements we found that the only effect on the kinetic profiles is to alter the intercept, but not the slope which is the relevant parameter. This is expected because the methanol concentration is in fact unaffected, since in all cases it is more than 5 orders of magnitude larger than that of formaldehyde.

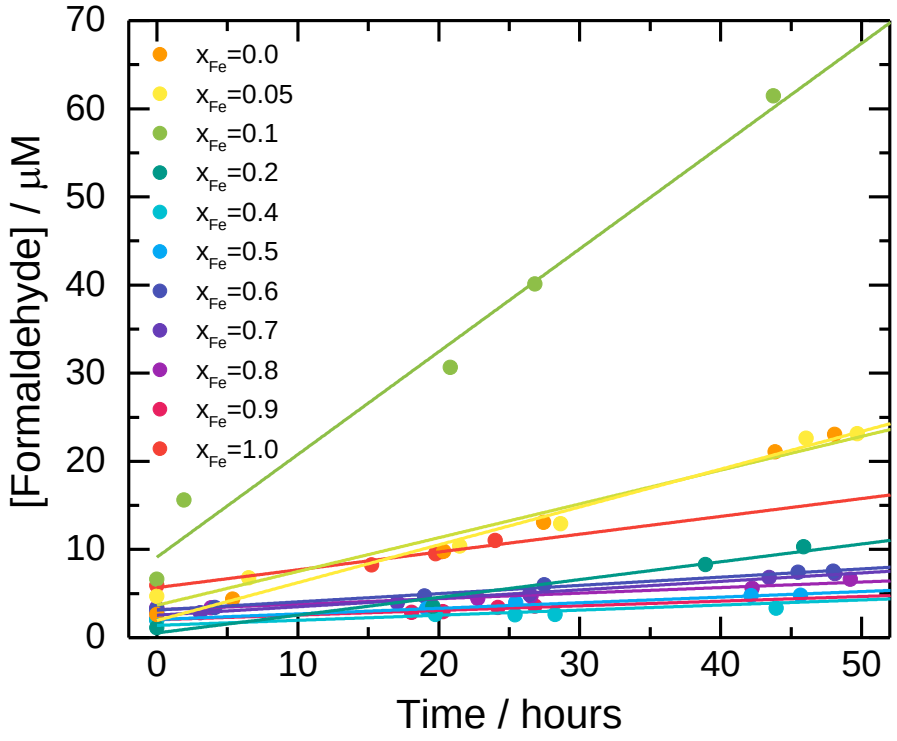

Figure 5: Kinetic profiles of formaldehyde formation by the visible-light photocatalytic oxidation of aqueous methanol using different members of the $Bi_2(Al_{1-x}Fe_x)_4O_9$ series of compounds. The lines show linear fits to the data.

The rate constants calculated by linear fits to the data are shown in Figure 6. As a general trend, the methanol oxidation process is significantly hindered by the incorporation of iron to the structure, with the x_{Fe} = 0.1 compound showing the largest rate constant and a *ca.* 7-

fold improvement over x_{Fe} = 1.0. For iron fractions larger than 0.3, the activity is negligible.

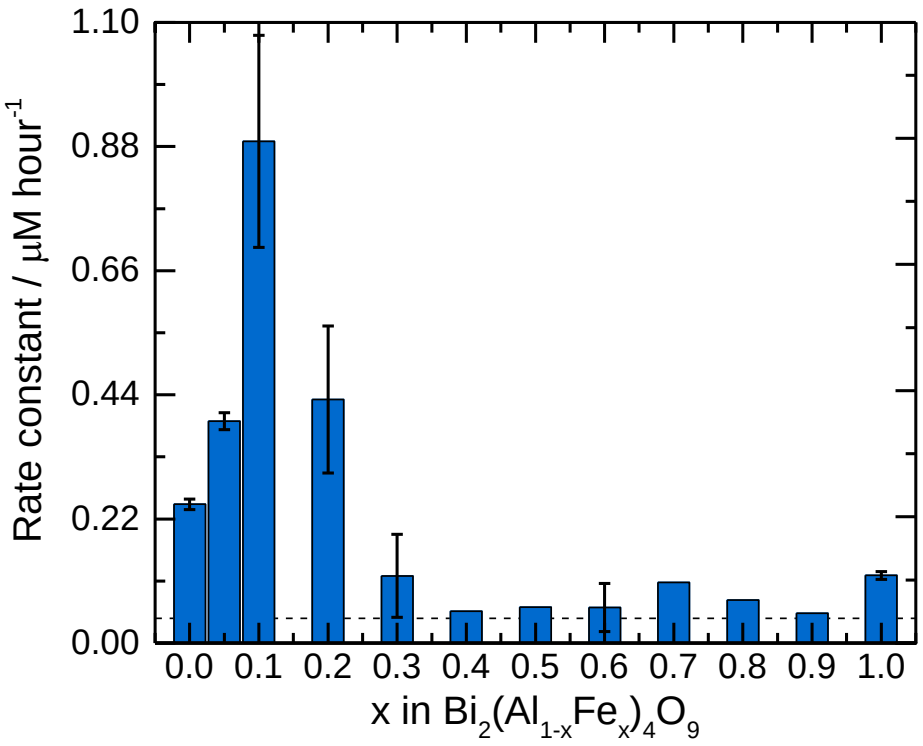

Figure 6: Rate constants for the photocatalytic oxidation of aqueous methanol obtained using the $Bi_2(Al_{1-x}Fe_x)_4O_9$ solid solutions. The dashed line represents the degradation rate constant for the blank experiment in the absence of photocatalyst. Error bars represent standard deviations.

We propose that the observed variation of the rate constant with the iron fraction can be satisfactorily explained by two opposing factors. On one hand, the incorporation of iron shifts the fundamental bandgap to lower energies. This means that the absorbed light fraction at the excitation wavelength (450 nm) increases with increasing x_{Fe} values. As an estimation of the absorbed light fraction we used $1 - R_{450}$ (where R_{450} is the absolute reflectance of the powders at 450 nm), assuming that all light is either reflected or

absorbed. These values, plotted versus x_{Fe}, are shown in Figure 8. The absorbed light fractions are close to unity for $0.2 < x_{Fe} < 1.0$, and abruptly decrease for $x_{Fe} < 0.2$, as expected from the reflectance spectra (Figure 2). On the other hand, the incorporation of iron shifts the conduction band edge towards more positive values, which could render the materials with high x_{Fe} unable to reduce O_2 (reaction (6d)). Moreover, the reduction of molecular oxygen by photogenerated electrons has been noted before to be the rate-determining step for the photocatalytic oxidation of methanol by TiO_2.[68]

In order to model the expected rate of electron transfer to O_2 for the different compounds, we employed the Marcus – Gerischer model:[69,70]

$$k_{ET} \propto exp\left[-\frac{(e\cdot E_{O_2/O_2^{\cdot-}} - \lambda - e\cdot E_{CB})^2}{4kT\lambda}\right] \quad (8)$$

Where k_{ET} is the rate constant for an electron transfer (ET) reaction, e the elementary charge, $E_{O_2/O_2^{\cdot-}}$ the one-electron reduction potential of O_2 under the reaction conditions (0.13 V vs. RHE for O_2/O_2^- at pH 7[58]), λ the reorganization energy (which can be assumed equal to 1.0 eV for the reduction of O_2[71]), E_{CB} the conduction band edge of the photocatalyst, k the Boltzmann constant, and T the temperature (assumed to be 298.15 K).

We must note that the flat-band potential not necessarily coincides with the conduction band edge. As discussed by Hankin et al.[72] the difference primarily depends on the charge carrier density and the effective mass of the electrons in the crystal lattice. Both parameters are ultimately related to the conductivity of the material,[73,74] and consequently the difference between the flat-band potential and the conduction band edge is negligible for doped or highly conductive materials, while significant in the case of low-conductivity materials.[21,75] The conductivity of $Bi_2Al_4O_9$ has been studied before, and although some controversies arose, conclusive evidence was brought forward showing a value of 10^{-7} S cm^{-1} at 873 K.[76,77] As discussed by Matsumoto,[75] the conduction band of materials with such low conductivities can be located at 0.4 V more negative potentials than their flat-band potential. Additionally, since we have determined the latter by the Mott – Schottky procedure, their values show comparatively large uncertainties. Therefore, in order to more clearly visualize the trend in the flat-band potentials we have fitted the measured values to an exponential function (blue line in Figure 4b). The position of the conduction band edges

was then modeled by shifting this function by 0.4 V towards the vacuum level, as explained above.

The exponential factors for the electron transfer rate calculated in this way from equation (8) are plotted in Figure 8. The same figure depicts the product of the fraction of absorbed light (1 – R) and the right-hand side of equation (8). Although the coincidence is not perfect, this product follows a very similar trend to that of the kinetic constants (Figure 6), showing that the aforementioned factors can be reasonably taken as the main variables affecting the photocatalytic activity of the different members of the solid solutions. The inter-sample variation in crystallinity, specific surface area, and presence of different phases, together with the simplification introduced when assuming the absorbed light fraction equal to 1-R, may explain the differences between Figure 6 and Figure 8. All in all, our analysis shows that a proper band-edge engineering is of fundamental importance for the design of visible-light responsive photocatalysts, perhaps above their light absorption properties.

In Figure 7 we show the conduction band potentials of the $Bi_2(Al_{1-x}Fe_x)_4O_9$ solid solutions, calculated by subtracting 0.4 V (as discussed above) to the measured flat-band potentials, together with the valence band potentials, calculated by adding the conduction band edge potentials to the bandgaps measured by means of the DASF method. While the trend of the former was already discussed, the latter remains, within the experimental error, constant along the different x_{Fe} values. This is consistent with the oxygen *2p* character assigned to the valence band of these compounds. It must be noted that the large uncertainty in the difference between the flat-band potential and the conduction band edge does not allow us to confidently assign error bars to the calculated values.

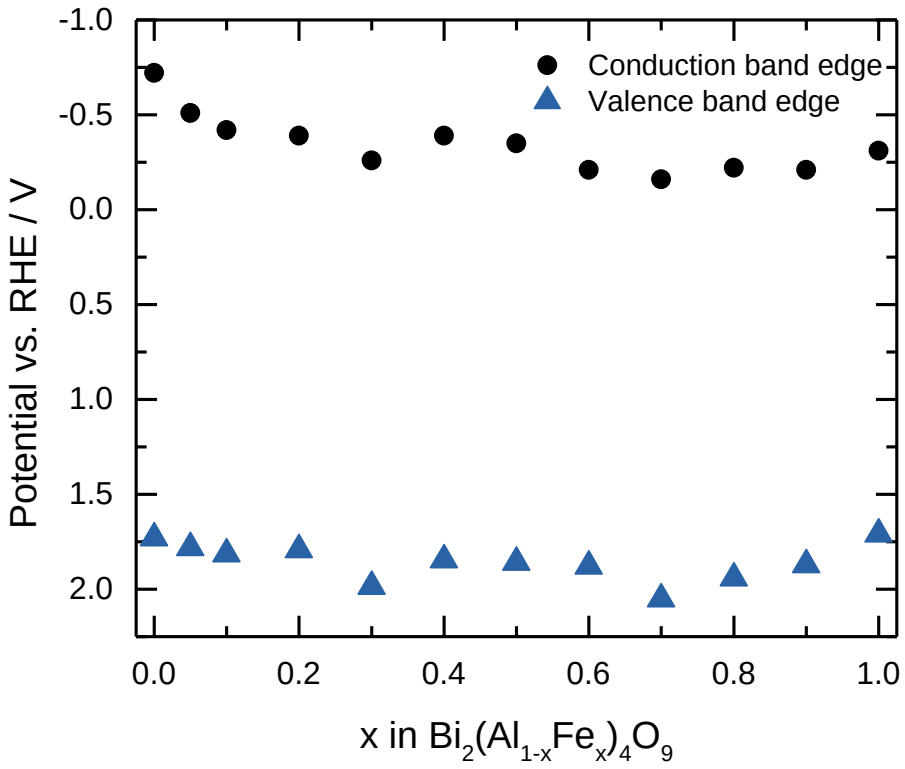

Figure 7: Conduction and valence band edge potentials of the $Bi_2(Al_{1-x}Fe_x)_4O_9$ compounds.

There are several examples in the literature where the photocatalytic activity of $Bi_2Fe_4O_9$ increases by the addition of hydrogen peroxide.[15,16,36,55] This enhancement has often been attributed to a photo-Fenton like reaction mechanism, though no conclusive evidence of it has been published. We note that, contrary to the O_2 reduction, the one-electron reduction potential of H_2O_2 (0.87 V vs. RHE at pH 7[78]) is well below the conduction band of $Bi_2Fe_4O_9$, and H_2O_2 can thus be readily reduced by the photogenerated electrons, as suggested by Wang et al.[36]. This may be, at least partially, the reason for the observed enhancement.

We would like to point out that the reaction rate constants (Figure 6) show rather low values. Taking into account an estimated light intensity of 80 mW cm^{-2}, the maximum observed photonic efficiency is around 0.01%. Eventual applications of this family of materials will require a significant step-up in its photocatalytic efficiency. In our opinion, there are two fundamental aspects that are worth exploring. Firstly, the average crystallite

size of $Bi_2Fe_4O_9$ has been shown to strongly affect its photocatalytic activity,[15,23] although the origin of such dependence is still unknown. A plausible explanation can be found in the chemically related hematite (α-Fe_2O_3), where the short hole diffusion length and long optical absorption depth result in the recombination of a large fraction of the photogenerated electron and holes.[79] Therefore, by analogy with hematite,[80,81] we propose that the preparation of colloidal $Bi_2(Al_{1-x}Fe_x)_4O_9$ nanoparticles, with a high specific surface area but more importantly with secondary particle sizes (i.e. aggregate sizes) around 20 nanometers could result in more efficient materials.

In second place, we have shown here that the incorporation of iron narrows the bandgap at the expense of lowering the reductive power of the photogenerated electrons. However, the incorporation of cocatalysts capable of reducing O_2 via multielectron transfers, such as Pt, may be able to circumvent this problem, thanks to a more positive potential for the multielectron reduction of O_2.[82]

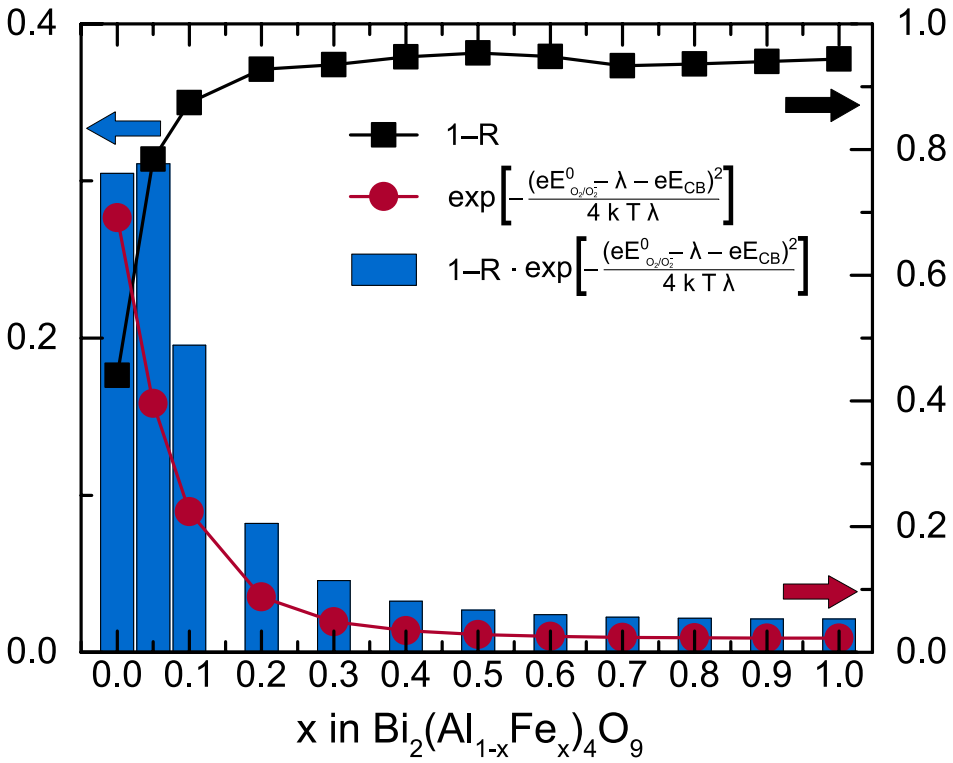

Figure 8: Representation of the fraction of absorbed light calculated as 1-R (where R is the absolute reflectance of the powders at 450 nm irradiation), the exponential factor of the Marcus – Gerischer model, and the product of both quantities.

4. Conclusions

We have synthesized 12 different members of the $Bi_2(Al_{1-x}Fe_x)_4O_9$ (x = 0 – 1) series of compounds following a previously reported procedure. By means of the Rietveld refinement of the X-ray diffraction patterns we show that the synthesis yields a mixture of mullite-type $Bi_2(Al_{1-x}Fe_x)_4O_9$ with varying amounts of perovskite-type $BiFeO_3$, β-Bi_2O_3, and Fe_3O_4. While the crystallinity of the compounds with low iron fractions is rather low, it steadily increases for larger iron fractions; the crystallite size remains practically constant within the 17–27 nm range. By performing a spectroscopic analysis based on the Derivation of Absorption Spectrum Fitting (DASF) and Tauc's methods we conclude that the fundamental bandgap decreases as iron is incorporated to the structure, while the electronic transitions switch from indirect for x_{Fe} = 0.0 to direct for x_{Fe} = 1.0. By means of the Mott–Schottky method we determined the flat-band potential of each member of the series, and observed that the incorporation of iron shifts the conduction band edge to potentials more positive vs. RHE than that of the one-electron reduction of O_2. We employed the oxidation of methanol under visible light irradiation as a reaction test to evaluate the photocatalytic activity of the materials, and found an optimal x_{Fe} value of 0.1. We explain the photocatalytic results on the basis of two opposing factors: while the incorporation of iron favors the absorption of visible light, it also lowers the conduction band edge, hindering the oxygen reduction half-reaction and thus promoting electron–hole recombination.

Acknowledgements

The authors acknowledge MINCYT-FONCYT (PICT 1456-2013) and UNMDP (EXA794/16) for the financial support. CBM is member of the research staff of Consejo Nacional de Investigaciones Científicas y Técnicas (CONICET). MC is grateful to

CONICET for his doctoral and postdoctoral fellowships, and to the MAPEX Center for Materials and Processes (University of Bremen) for the Research stay. The authors would like to thank Iván Berengeno (UNMdP) for his help setting up the photocatalytic reaction, and Joaquín H. Ubogui, Paula Cecilia dos Santos Claro, and Antonela Cánneva (YPF Tecnología S. A.) for the XPS spectra and HRTEM micrographs. LIG acknowledges the Niedersächsisches Ministerium für Wissenschaft und Kultur (NTH-research group "ElektroBak") for the financial support. Finally, we would like to thank the Deutsche Forschungsgemeinschaft (DFG) for financial support in the large scientific instrument program (University of Bremen, INST 144/435-1 FUGG).

Supporting Information

The Supporting Information file contains the XRD patterns, the amount of reagents used for each synthesis, SEM micrographs of the powders and films, TEM micrographs of the powders, XPS spectra, the emission spectrum of the light source for the photocatalytic experiments, and the calculations of the bandgap for sample x_{Fe}=1.0 using the Tauc's and DASF methods.

References

(1) Frank, S. N.; Bard, A. J. Heterogeneous Photocatalytic Oxidation of Cyanide Ion in Aqueous Solutions at TiO_2 Powder. *J. Am. Chem. Soc.* **1977**, *99*, 303–304.

(2) Gaya, U. I.; Abdullah, A. H. Heterogeneous Photocatalytic Degradation of Organic Contaminants over Titanium Dioxide: A Review of Fundamentals, Progress and Problems. *J. Photochem. Photobiol. C* **2008**, *9*, 1–12.

(3) Asahi, R.; Morikawa, T.; Irie, H.; Ohwaki, T. Nitrogen-Doped Titanium Dioxide as Visible-Light-Sensitive Photocatalyst: Designs, Developments, and Prospects. *Chem. Rev.* **2014**, *114*, 9824–9852.

(4) Fischer, R. X.; Schneider, H. *Mullite*; Schneider, H., Komarneni, S., Eds.; John Wiley & Sons, 2005.

(5) Gesing, T. M.; Fischer, R. X.; Burianek, M.; Mühlberg, M.; Debnath, T.; Rüscher, C. H.; Ottinger, J.; Buhl, J. C.; Schneider, H. Synthesis and Properties of Mullite-Type $(Bi_{1-x}Sr_x)_2(M^1_{1-y}M^2_y)_4O_{9-x}$ (M=Al, Ga, Fe). *J. Eur. Ceram. Soc.* **2011**, *31*, 3055–3062.

(6) Schneider, H.; Fischer, R. X.; Gesing, T. M.; Schreuer, J.; Muhlberg, M. Crystal

Chemistry and Properties of Mullite-Type $Bi_2M_4O_9$: An Overview. *Int. J. Mater. Res.* **2012**, *103*, 422–429.

(7) Weber, S.-U.; Gesing, T. M.; Röder, J.; Litterst, F. J.; Fischer, R. X.; Becker, K.-D. Temperature-Dependent ^{57}Fe Mössbauer Spectroscopy and Local Structure of Mullite-Type $Bi_2(Fe_xAl_{1-x})_4O_9$ ($0.1 \leq x \leq 1$) Solid Solutions. *Int. J. Mater. Res.* **2012**, *103*, 430–437.

(8) Weber, S.; Gesing, T. M.; Eckold, G.; Fischer, R. X.; Litterst, F.; Becker, K. Temperature-Dependent ^{57}Fe Mössbauer Spectroscopy and Local Structure of the Mullite Type $Bi_2(Fe_xGa_{1-x})_4O_9$ ($0.1<x<1$). *J. Phys. Chem. Solids* **2014**, *75*, 416–426.

(9) Kirsch, A.; Murshed, M. M.; Gaczynski, P.; Becker, K. D.; Gesing, T. M. $Bi_2Fe_4O_9$: Structural Changes from Nano-to Micro-Crystalline State. *Z. Naturforsch.* **2016**, *71*, 447–455.

(10) Murshed, M. M.; Nénert, G.; Burianek, M.; Robben, L.; Mühlberg, M.; Schneider, H.; Fischer, R. X.; Gesing, T. M. Temperature-Dependent Structural Studies of Mullite-Type $Bi_2Fe_4O_9$. *J. Solid State Chem.* **2013**, *197*, 370–378.

(11) Ressouche, E.; Simonet, V.; Canals, B.; Gospodinov, M.; Skumryev, V. Magnetic Frustration in an Iron-Based Cairo Pentagonal Lattice. *Phys. Rev. Lett.* **2009**, *103*, 267204.

(12) Curti, M.; Gesing, T. M.; Murshed, M. M.; Bredow, T.; Mendive, C. B. Liebau Density Vector: A New Approach to Characterize Lone Electron Pairs in Mullite-Type Materials. *Zeitschrift für Krist. - Cryst. Mater.* **2013**, *228*.

(13) Kirsch, A.; Murshed, M. M.; Schowalter, M.; Rosenauer, A.; Gesing, T. M. Nanoparticle Precursor into Polycrystalline $Bi_2Fe_4O_9$: An Evolutionary Investigation of Structural, Morphological, Optical, and Vibrational Properties. *J. Phys. Chem. C* **2016**, *120*, 18831–18840.

(14) Bahnemann, D. Catalysis Letters: Editorial. *Catal. Letters* **2017**, *147*, 2473–2474.

(15) Sun, S.; Wang, W.; Zhang, L.; Shang, M. Visible Light-Induced Photocatalytic Oxidation of Phenol and Aqueous Ammonia in Flowerlike $Bi_2Fe_4O_9$ Suspensions. *J. Phys. Chem. C* **2009**, *113*, 12826–12831.

(16) Hu, Z.-T.; Chen, B.; Lim, T.-T. Single-Crystalline $Bi_2Fe_4O_9$ Synthesized by Low-Temperature Co-Precipitation: Performance as Photo- and Fenton Catalysts. *RSC Adv.* **2014**, *4*, 27820.

(17) Bae, S.; Kim, S.; Lee, S.; Choi, W. Dye Decolorization Test for the Activity Assessment of Visible Light Photocatalysts: Realities and Limitations. *Catal. Today* **2014**, *224*, 21–28.

(18) Yan, X.; Ohno, T.; Nishijima, K.; Abe, R.; Ohtani, B. Is Methylene Blue an Appropriate Substrate for a Photocatalytic Activity Test? A Study with Visible-Light Responsive Titania. *Chem. Phys. Lett.* **2006**, *429*, 606–610.

(19) Ohtani, B. Revisiting the Original Works Related to Titania Photocatalysis: A Review of Papers in the Early Stage of Photocatalysis Studies. *Electrochemistry* **2014**, *82*, 414–425.

(20) Rochkind, M.; Pasternak, S.; Paz, Y. Using Dyes for Evaluating Photocatalytic Properties: A Critical Review. *Molecules* **2015**, *20*, 88–110.

(21) Beranek, R. (Photo)Electrochemical Methods for the Determination of the Band Edge Positions of TiO_2-Based Nanomaterials. *Adv. Phys. Chem.* **2011**, *2011*, 1–20.

(22) Teck, M.; Murshed, M. M.; Schowalter, M.; Lefeld, N.; Grossmann, H. K.; Grieb, T.; Hartmann, T.; Robben, L.; Rosenauer, A.; Mädler, L.; Gesing, T. M. Structural

and Spectroscopic Comparison between Polycrystalline, Nanocrystalline and Quantum Dot Visible Light Photo-Catalyst Bi_2WO_6. *J. Solid State Chem.* **2017**, *254*, 82–89.

(23) Zhang, Q.; Gong, W.; Wang, J.; Ning, X.; Wang, Z.; Zhao, X.; Ren, W.; Zhang, Z. Size-Dependent Magnetic, Photoabsorbing, and Photocatalytic Properties of Single-Crystalline $Bi_2Fe_4O_9$ Semiconductor Nanocrystals. *J. Phys. Chem. C* **2011**, *115*, 25241–25246.

(24) Carpenter, J. H. New Measurements of Oxygen Solubility in Pure and Natural Water. *Limnol. Oceanogr.* **1966**, *11*, 264–277.

(25) Nash, T. The Colorimetric Estimation of Formaldehyde by Means of the Hantzsch Reaction. *Biochem. J.* **1953**, *55*, 416–421.

(26) Goldstein, S.; Behar, D.; Rabani, J. Mechanism of Visible Light Photocatalytic Oxidation of Methanol in Aerated Aqueous Suspensions of Carbon-Doped TiO_2. *J. Phys. Chem. C* **2008**, *112*, 15134–15139.

(27) Wang, C. Y.; Pagel, R.; Bahnemann, D. W.; Dohrmann, J. K. Quantum Yield of Formaldehyde Formation in the Presence of Colloidal TiO2-Based Photocatalysts: Effect of Intermittent Illumination, Platinization, and Deoxygenation. *J. Phys. Chem. B* **2004**, *108*, 14082–14092.

(28) Rietveld, H. M. A Profile Refinement Method for Nuclear and Magnetic Structures. *J. Appl. Crystallogr.* **1969**, *2*, 65–71.

(29) Voll, D.; Beran, A.; Schneider, H. Variation of Infrared Absorption Spectra in the System $Bi_2Al_{4-x}Fe_xO_9$ (x = 0–4), Structurally Related to Mullite. *Phys. Chem. Miner.* **2006**, *33*, 623–628.

(30) Shannon, R. D. Revised Effective Ionic Radii and Systematic Studies of Interatomic Distances in Halides and Chalcogenides. *Acta Crystallogr. A* **1976**, *32*, 751–767.

(31) Vegard, L. Die Konstitution Der Mischkristalle Und Die Raumfüllung Der Atome. *Zeitschrift für Phys.* **1921**, *5*, 17–26.

(32) Valant, M.; Axelsson, A.; Alford, N. Peculiarities of a Solid-State Synthesis of Multiferroic Polycrystalline $BiFeO_3$. *Chem. Mater.* **2007**, *19*, 5431–5436.

(33) Selbach, S. M.; Einarsrud, M.-A.; Grande, T. On the Thermodynamic Stability of $BiFeO_3$. *Chem. Mater.* **2009**, *21*, 169–173.

(34) Gesing, T. M.; Schowalter, M.; Weidenthaler, C.; Murshed, M. M.; Nénert, G.; Mendive, C. B.; Curti, M.; Rosenauer, A.; Buhl, J.-C.; Schneider, H.; Fischer, R. X. Strontium Doping in Mullite-Type Bismuth Aluminate: A Vacancy Investigation Using Neutrons, Photons and Electrons. *J. Mater. Chem.* **2012**, *22*.

(35) Hu, Z. T.; Liu, J.; Yan, X.; Oh, W. Da; Lim, T. T. Low-Temperature Synthesis of Graphene/$Bi_2Fe_4O_9$ Composite for Synergistic Adsorption-Photocatalytic Degradation of Hydrophobic Pollutant under Solar Irradiation. *Chem. Eng. J.* **2015**, *262*, 1022–1032.

(36) Wang, X.; Zhang, M.; Tian, P.; Chin, W. S.; Zhang, C. M. A Facile Approach to Pure-Phase $Bi_2Fe_4O_9$ Nanoparticles Sensitive to Visible Light. *Appl. Surf. Sci.* **2014**, *321*, 144–149.

(37) Gao, K.; Zhu, J.; Gu, X.; Xie, Q.; Zhang, F.; Wu, X. Synthesis and Properties of $Bi_2Fe_4O_9$ with $FeCl_2 \cdot 6H_2O$ Addition. *J. Am. Ceram. Soc.* **2015**, *98*, 1128–1132.

(38) Kubelka, P. New Contributions to the Optics of Intensely Light-Scattering Materials Part I. *J. Opt. Soc. Am.* **1948**, *38*, 448.

(39) Zhang, Y.; Guo, Y.; Duan, H.; Li, H.; Yang, L.; Wang, P.; Sun, C.; Xu, B.; Liu, H.

Photoelectrochemical Response and Electronic Structure Analysis of Mono-Dispersed Cuboid-Shaped $Bi_2Fe_4O_9$ Crystals with near-Infrared Absorption. *RSC Adv.* **2014**, *4*, 28209–28218.

(40) Sherman, D. M.; Waite, T. D. Electronic Spectra of Fe^{3+} Oxides and Oxide Hydroxides in the near IR to near UV. *Am. Mineral.* **1985**, *70*, 1262–1269.

(41) Curti, M.; Granone, L.; Gesing, T. M.; Murshed, M. M.; Bredow, T.; Mendive, C. B. International Center for Computational Materials Science-Workshop Functional Oxides for Emerging Technologies. **2013**, Bremen, Germany.

(42) Zahedi, E.; Xiao, B.; Shayestefar, M. First-Principles Investigations of the Structure, Electronic, and Optical Properties of Mullite-Type Orthorhombic $Bi_2M_4O_9$ (M = Al^{3+}, Ga^{3+}). *Inorg. Chem.* **2016**, *55*, 4824–4835.

(43) Tauc, J.; Grigorovici, R.; Vancu, A. Optical Properties and Electronic Structure of Amorphous Germanium. *Phys. Status Solidi* **1966**, *15*, 627–637.

(44) Tauc, J. Optical Properties and Electronic Structure of Amorphous Ge and Si. *Mater. Res. Bull.* **1968**, *3*, 37–46.

(45) Souri, D.; Tahan, Z. E. A New Method for the Determination of Optical Band Gap and the Nature of Optical Transitions in Semiconductors. *Appl. Phys. B* **2015**, *119*, 273–279.

(46) Scaife, D. E. Oxide Semiconductors in Photoelectrochemical Conversion of Solar Energy. *Sol. Energy* **1980**, *25*, 41–54.

(47) Ohtani, B. Photocatalysis A to Z—What We Know and What We Do Not Know in a Scientific Sense. *J. Photochem. Photobiol. C* **2010**, *11*, 157–178.

(48) Mohapatra, S. R.; Sahu, B.; Kaushik, S. D.; Singh, A. K. Effect of Co Doping on Structural, Optical, Magnetic and Dielectric Properties of $Bi_2Fe_4O_9$. In *AIP Conference Proceedings*; 2015; Vol. 1665, pp 140034-1–3.

(49) Ruan, Q.-J.; Zhang, W.-D. Tunable Morphology of $Bi_2Fe_4O_9$ Crystals for Photocatalytic Oxidation. *J. Phys. Chem. C* **2009**, *113*, 4168–4173.

(50) Irshad, Z.; Shah, S. H.; Rafiq, M. A.; Hasan, M. M. First Principles Study of Structural, Electronic and Magnetic Properties of Ferromagnetic $Bi_2Fe_4O_9$. *J. Alloys Compd.* **2015**, *624*, 131–136.

(51) Peiró, A. M.; Colombo, C.; Doyle, G.; Nelson, J.; Mills, A.; Durrant, J. R. Photochemical Reduction of Oxygen Adsorbed to Nanocrystalline TiO2 Films: A Transient Absorption and Oxygen Scavenging Study of Different TiO2 Preparations. *J. Phys. Chem. B* **2006**, *110*, 23255–23263.

(52) Gheorghiu, F.; Tanasa, R.; Buscaglia, M. T.; Buscaglia, V.; Pastravanu, C. G.; Popovici, E.; Mitoseriu, L. Preparation of $Bi_2Fe_4O_9$ Particles by Hydrothermal Synthesis and Functional Properties. *Phase Transitions* **2013**, *86*, 726–736.

(53) Liu, Z.; Wu, B.; Yin, D.; Zhu, Y.; Wang, L. Enhanced Photocatalytic Activity in Al-Substituted $Bi_2Fe_4O_9$ Submicrocrystals. *J. Mater. Sci.* **2012**, *47*, 6777–6783.

(54) Liu, Z.; Wu, B.; Zhu, Y. Microwave Hydrothermal Synthesis of $Bi_2Fe_4O_9$ Crystals with Visible Light Photocatalytic Activity. *Mater. Chem. Phys.* **2012**, *135*, 474–478.

(55) Qi, S.; Zuo, R.; Wang, Y.; Chan, H. W. L. Synthesis and Photocatalytic Performance of the Electrospun $Bi_2Fe_4O_9$ Nanofibers. *J. Mater. Sci.* **2013**, *48*, 4143–4150.

(56) Peter, L. M.; Tributsch, H. Experimental Techniques in Photoelectrochemistry. In *Nanostructured and Photoelectrochemical Systems for Solar Photon Conversion*; 2009; pp 675–736.

(57) Raebiger, H.; Lany, S.; Zunger, A. Origins of the P-Type Nature and Cation

Deficiency in Cu_2O and Related Materials. *Phys. Rev. B* **2007**, *76*, 1–5.

(58) Bard, A. J.; Parsons, R.; Jordan, J.; Chemistry., I. U. of P. and A. *Standard Potentials in Aqueous Solution*; M. Dekker: New York, 1985.

(59) Baumanis, C.; Bloh, J. Z.; Dillert, R.; Bahnemann, D. W. Hematite Photocatalysis: Dechlorination of 2,6-Dichloroindophenol and Oxidation of Water. *J. Phys. Chem. C* **2011**, *115*, 25442–25450.

(60) Kennedy, J. H. Flatband Potentials and Donor Densities of Polycrystalline α-Fe_2O_3 Determined from Mott-Schottky Plots. *J. Electrochem. Soc.* **1978**, *125*, 723.

(61) Hunt, P.; Sprik, M. On the Position of the Highest Occupied Molecular Orbital in Aqueous Solutions of Simple Ions. *ChemPhysChem* **2005**, *6*, 1805–1808.

(62) Esch, T. R.; Bredow, T. Band Positions of Rutile Surfaces and the Possibility of Water Splitting. *Surf. Sci.* **2017**, *665*, 20–27.

(63) Puga, A. V. Photocatalytic Production of Hydrogen from Biomass-Derived Feedstocks. *Coord. Chem. Rev.* **2016**, *315*, 1–66.

(64) Hoffmann, M. R.; Hoffmann, M. R.; Martin, S. T.; Martin, S. T.; Choi, W.; Choi, W.; Bahnemannt, D. W.; Bahnemannt, D. W. Environmental Applications of Semiconductor Photocatalysis. *Chem. Rev.* **1995**, *95*, 69–96.

(65) Melcher, J.; Feroz, S.; Bahnemann, D. Comparing Photocatalytic Activities of Commercially Available Iron-Doped and Iron-Undoped Aeroxide TiO_2 P25 Powders. *J. Mater. Sci.* **2017**, *52*, 6341–6348.

(66) Chiarello, G. L.; Ferri, D.; Selli, E. Effect of the CH_3OH/H_2O Ratio on the Mechanism of the Gas-Phase Photocatalytic Reforming of Methanol on Noble Metal-Modified TiO_2. *J. Catal.* **2011**, *280*, 168–177.

(67) Dimitrijevic, N. M.; Shkrob, I. A.; Gosztola, D. J.; Rajh, T. Dynamics of Interfacial Charge Transfer to Formic Acid, Formaldehyde, and Methanol on the Surface of TiO_2 Nanoparticles and Its Role in Methane Production. *J. Phys. Chem. C* **2012**, *116*, 878–885.

(68) Wang, C. yi; Rabani, J.; Bahnemann, D. W.; Dohrmann, J. K. Photonic Efficiency and Quantum Yield of Formaldehyde Formation from Methanol in the Presence of Various TiO_2 Photocatalysts. *J. Photochem. Photobiol. A* **2002**, *148*, 169–176.

(69) Marcus, R. A. On the Theory of Oxidation-Reduction Reactions Involving Electron Transfer. I. *J. Chem. Phys.* **1956**, *24*, 966–978.

(70) Gerischer, H. Charge Transfer Processes at Semiconductor-Electrolyte Interfaces in Connection with Problems of Catalysis. *Surf. Sci.* **1969**, *18*, 97–122.

(71) Gerischer, H.; Heller, A. The Role of Oxygen in Photooxidation of Organic Molecules on Semiconductor Particles. *J. Phys. Chem.* **1991**, *95*, 5261–5267.

(72) Hankin, A.; Alexander, J. C.; Kelsall, G. H. Constraints to the Flat Band Potential of Hematite Photo-Electrodes. *Phys. Chem. Chem. Phys.* **2014**, *16*, 16176–16186.

(73) Matsumoto, Y. Photoelectrochemical Properties of the Zn-Ti-Fe Spinel Oxides. *J. Electrochem. Soc.* **1986**, *133*, 711.

(74) Matsumoto, Y.; Sugiyama, K.; Sato, E. I. Improvement of $CaFe_2O_4$ Photocathode by Doping with Na and Mg. *J. Solid State Chem.* **1988**, *74*, 117–125.

(75) Matsumoto, Y. Energy Positions of Oxide Semiconductors and Photocatalysis with Iron Complex Oxides. *J. Solid State Chem.* **1996**, *126*, 227–234.

(76) Ohmann, S.; Fielitz, P.; Dörrer, L.; Borchardt, G.; Gesing, T. M.; Fischer, R. X.; Rüscher, C. H.; Buhl, J.-C.; Becker, K.-D.; Schneider, H. Electrical Conductivity of Mullite-Type $Bi_2Al_4O_9$ Ceramics in Air. *Solid State Ionics* **2012**, *211*, 46–50.

(77) Larose, S.; Akbar, S. A. Synthesis and Electrical Properties of Dense $Bi_2Al_4O_9$. *J. Solid State Electrochem.* **2006**, *10*, 488–498.
(78) Wardman, P. Reduction Potentials of One-Electron Couples Involving Free Radicals in Aqueous Solution. *J. Phys. Chem. Ref. Data* **1989**, *18*, 1637–1755.
(79) Barroso, M.; Pendlebury, S.; Cowan, A.; Durrant, J. R. Charge Carrier Trapping, Recombination and Transfer in Hematite (α-Fe_2O_3) Water Splitting Photoanodes. *Chem. Sci.* **2013**, *4*, 2724–2734.
(80) Townsend, T. K.; Sabio, E. M.; Browning, N. D.; Osterloh, F. E. Photocatalytic Water Oxidation with Suspended Alpha-Fe_2O_3 Particles-Effects of Nanoscaling. *Energy Environ. Sci.* **2011**, *4*, 4270.
(81) Klahr, B. M.; Martinson, A. B. F.; Hamann, T. W. Photoelectrochemical Investigation of Ultrathin Film Iron Oxide Solar Cells Prepared by Atomic Layer Deposition. *Langmuir* **2011**, *27*, 461–468.
(82) Abe, R.; Takami, H.; Murakami, N.; Ohtani, B. Pristine Simple Oxides as Visible Light Driven Photocatalysts: Highly Efficient Decomposition of Organic Compounds over Platinum-Loaded Tungsten Oxide. *J. Am. Chem. Soc.* **2008**, *130*, 7780–7781.